Journal of Computational Physics 409 (2020) 109316

Contents lists available at ScienceDirect

Journal of Computational Physics

www.elsevier.com/locate/jcp

Multiscale mixed methods for two-phase flows in high-contrast porous media

Franciane F. Rocha [a], Fabricio S. Sousa [a,*], Roberto F. Ausas [a], Gustavo C. Buscaglia [a], Felipe Pereira [b]

[a] Instituto de Ciências Matemáticas e de Computação, Universidade de São Paulo, Av. Trabalhador São-carlense, 400, 13566-590, São Carlos, SP, Brazil
[b] Department of Mathematical Sciences, The University of Texas at Dallas, 800 W. Campbell Road, Richardson, TX 75080-3021, USA

ARTICLE INFO

Article history:
Received 29 April 2019
Received in revised form 19 November 2019
Accepted 5 February 2020
Available online 14 February 2020

Keywords:
Multiscale Robin Coupled Method
Domain decomposition
Multiscale methods
Two-phase flows
High-contrast porous media

ABSTRACT

The Multiscale Robin Coupled Method (MRCM) is a domain decomposition procedure that has been developed to efficiently approximate velocity and pressure fields for single-phase flows in highly heterogeneous porous media. It generalizes other well-established multiscale domain decomposition mixed methods and it adds great flexibility to the choice of interface spaces as well as in the boundary conditions for subdomain coupling. We investigate the approximation of two phase flows in porous media using the MRCM to compute velocity fields. We consider an operator splitting strategy, where a scalar conservation law for the saturation of one of the phases and the velocity field are updated sequentially. We find that the coupling of nearest neighbor subdomains through the imposition of a continuous pressure (respectively, normal fluxes) is the best strategy to approximate two-phase flows in the presence of high (resp., low) permeability channels (resp., regions). A new adaptivity strategy for setting an algorithmic parameter of the MRCM, that controls the relative importance of Dirichlet and Neumann boundary conditions in the coupling of subdomains, is proposed and tested in challenging, high-contrast permeability fields. Our numerical simulations of two-phase flows show that by switching between existing multiscale procedures we can observe unprecedented accuracy, in that we produce better solutions for problems with high-contrast permeability coefficients when compared to solutions obtained with some standard multiscale mixed methods.

1. Introduction

Problems of interest to the industry today involve several billion cells and thousands of time steps. Traditional simulation techniques developed for serial calculations cannot handle effectively problems of such magnitude. Multiscale methods aim at reducing the computational complexity of the numerical simulation of such problems by decomposing large computational tasks in a family of smaller problems that can be solved simultaneously in state-of-the-art parallel machines. These methods have received considerable attention of several groups. See [1] for a very comprehensive comparison of procedures

* Corresponding author.
E-mail addresses: fr.franciane@usp.br (F.F. Rocha), fsimeoni@icmc.usp.br (F.S. Sousa), rfausas@icmc.usp.br (R.F. Ausas), gustavo.buscaglia@icmc.usp.br (G.C. Buscaglia), felipepereira62@gmail.com (F. Pereira).

https://doi.org/10.1016/j.jcp.2020.109316
0021-9991/

of this type. Multiscale methods have been developed in the framework of the finite volume, finite element and mixed finite element methods.

The multiscale procedures based on the finite volume method [2,3] were firstly proposed to solve elliptic problems arising in two-phase flows and then extended to complex physics and fractures (see [4–6] and references therein). The finite element approach, introduced in [7], has been used to solve elliptic problems and applied to composite materials as well as to flows in porous media [8]. The variational [9], the generalized [10] and the hybrid [11] finite element approximations have been also introduced. Applications to complex domains, possibly including fractures, are presented in [12–15] among many others.

Here we focus on multiscale mixed finite element methods. One of these procedures that has been recently proposed is the Multiscale Robin Coupled Method (MRCM) [16,17] which is based on a domain decomposition described in [18] and on the Multiscale Mixed Method (MuMM) [19]. The domain decomposition of the MRCM considers weak continuity of normal fluxes and pressures through the imposition of Robin boundary conditions. The MRCM can be seen as a generalization of the Multiscale Mortar Mixed Finite Element Method (MMMFEM) [20] and the Multiscale Hybrid-Mixed Finite Element Method (MHM) [21,22]. In the MMMFEM the pressure continuity is satisfied in the fine-grid scale, while normal flux continuity is ensured weakly on a larger scale. In the MHM the continuity of the normal flux is satisfied at the fine-grid scale and the pressure continuity is imposed weakly on a larger scale. Other well known multiscale methods based on mixed finite elements are presented in [23–25].

Several multiscale methods have been used to approximate two-phase flows in high-contrast heterogeneous porous media. Developments with the MMMFEM can be found in [26,27], while examples of two-phase flows with other multiscale methods can be found in [28–31] and references therein. Aiming at coupling flow and transport equations both operator splitting techniques [32–35] and fully implicit formulations [36,37] have also been considered.

In this work we focus on two-phase (oil-water) immiscible displacement in high-contrast porous media. The governing system of equations is approximated by an operator splitting scheme, as presented in [38–40]. We combine the MRCM for the approximation of Darcy's velocity with a finite volume method to approximate the hyperbolic conservation law for the water saturation. Any hyperbolic solver can be combined with the MRCM. Different schemes for this transport equation have been used in the approximation of flows through porous media. For example, the upwind method (considered in [3,33,41]), high order variations of the Godunov method [42] and central schemes [43]. In this paper we consider the central scheme Kurganov-Tadmor [44,45], which is known to produce robust approximations along with accurate numerical solutions.

We find that the coupling of adjacent subdomains through the imposition of a continuous pressure is the best strategy to approximate two-phase flows in the presence of high permeability channels; such coupling can be implemented by the MMMFEM. On the other hand, the coupling of subdomains through the imposition of continuous normal components of fluxes is an adequate strategy to handle low permeability regions; this can be accomplished by the use of the MHM. Thus, accuracy in the approximation of two-phase flows would require that, adaptively, the numerical procedure to solve for velocity and pressure switches between the MMMFEM and MHM, depending on the underlying heterogeneity (given by the product of the total mobility and absolute permeability of the problem at hand). A method that allows one to switch between the MMMFEM and MHM locally in the skeleton of the domain decomposition is not known. However, such task is easily accomplished if one takes advantage of a built-in algorithmic parameter of the MRCM, that allows this method to produce either MMMFEM-like or MHM-like solutions, by setting this parameter to extreme values. To the best knowledge of the authors the MRCM is the only multiscale procedure that has this flexibility to switch from Dirichlet-dominated to Neumann-dominated coupling of subdomains; a new adaptive scheme based on this idea is proposed and tested through several numerical simulations of two-phase flows in high-contrast formations. We show that the MRCM can produce considerably more accurate solutions than some standard multiscale methods. We remark that the concept of adaptivity has been very recently applied in the numerical approximation of two-phase flows [6], where improved accuracy in numerical solutions requires the construction of special multiscale basis functions adapted to the underlying heterogeneity.

The paper is organized as follows. In Section 2 the governing equations describing two-phase flows in porous media are presented. Then, in Section 3 we present the operator splitting scheme that we use in the approximation of two-phase flows and we recall the MRCM, the method of our choice to solve for velocity and pressure. Numerical simulation results of two-phase flows are presented and carefully discussed in Section 4; initially we compare multiscale procedures in terms of norms that measure global quantities. Then, we perform a detailed analysis of the approximation of fingering instabilities. Finally, we present our conclusions and plans for future work in Section 5. The Kurganov-Tadmor scheme for hyperbolic conservation laws appears in the Appendix A.

2. Mathematical setting

We consider immiscible and incompressible two-phase flow of water and oil (denoted by w and o, respectively) in a heterogeneous reservoir. For simplicity, a fully saturated regime is considered, meaning that the sum of both oil and water saturation is equal to one, while other effects such capillary pressure and gravity are neglected. The resulting differential equations for this model consists of the Darcy's law with a statement of conservation of mass, given by

$$\nabla \cdot \mathbf{u} = q, \qquad \mathbf{u} = -\lambda(s) K(\mathbf{x}) \nabla p, \tag{1}$$

Algorithm 1 Solving equations (1)-(2) by operator splitting.

1: Given $s^n(\mathbf{x})$, $p^n(\mathbf{x})$ and $\mathbf{u}^n(\mathbf{x})$ computed from previous time step
2: **for** $k = 1$ **to** C **do**
3: $t_{n,k} = t_n + k\Delta t_s$
4: Compute $\mathbf{u}^e(\mathbf{x}, t_{n,k})$ from Eq. (4)
5: Solve Eq. (2) with $\mathbf{u} = \mathbf{u}^e$ to compute $s(\mathbf{x}, t_{n,k})$ using the KT method
6: **end for**
7: Given $s^{n+1}(\mathbf{x})$, update $\kappa = \lambda(s^{n+1}(\mathbf{x}))K(\mathbf{x})$
8: Solve Eq. (1) to obtain $p^{n+1}(\mathbf{x})$ and $\mathbf{u}^{n+1}(\mathbf{x})$ using the MRCM
9: Make $n \leftarrow n+1$ and return to step 1

coupled with the hyperbolic conservation law for the transport of water saturation [46,47], which is given by

$$\frac{\partial s}{\partial t} + \nabla \cdot (f(s)\mathbf{u}) = 0. \tag{2}$$

Here $\mathbf{u}(\mathbf{x}, t)$ is the Darcy velocity, $s(\mathbf{x}, t)$ represents the water saturation, $K(\mathbf{x})$ is the absolute permeability and $p(\mathbf{x}, t)$ is the pressure. Both the total mobility $\lambda(s) = \lambda_w(s) + \lambda_o(s)$ and the fractional flow of water $f(s)$ functions are respectively given by

$$\lambda(s) = \frac{k_{rw}(s)}{\mu_w} + \frac{k_{ro}(s)}{\mu_o} \qquad \text{and} \qquad f(s) = \frac{\lambda_w(s)}{\lambda(s)}, \tag{3}$$

where $k_{rj}(s)$ and μ_j, $j \in \{w, o\}$, are respectively the given relative permeability function and viscosity of phase j. For simplicity we assume a constant porosity and it has been scaled out by changing the time variable.

To complete the mathematical model, an initial condition for saturation and boundary data for pressure or normal fluxes are required, usually taking into account injection and production wells, such that water is injected to displace the trapped oil towards the production wells. These conditions will be detailed in the next section.

3. Numerical approximation

In this work, the coupled system of model equations (1)-(2), along with suitable boundary and initial conditions, will be solved by a popular technique of operator splitting. Since both equations are very different in nature, being (1) elliptic and (2) hyperbolic, it is only natural to split the computation of both these equations in time, taking advantage of the specific methods developed for each class of equations. We are particularly interested in using the Multiscale Robin Coupled method to solve equation (1), while the transport of saturation modeled by equation (2) will be handled by a well known scheme for hyperbolic conservation laws, the Kurganov-Tadmor (KT) method [44,45] (see Appendix A).

3.1. Handling different time steps

Another advantage of splitting equations (1)-(2) is that efficiency in the computation of the solution can be improved, usually considering larger time steps for the pressure equation (1) compared to those used for the hyperbolic equation (2), where CFL-type condition is enforced to ensure numerical stability of explicit schemes (more details can be found in [38–40]).

Let Δt_s be the time step used in the discretization of the saturation equation, and let Δt_p be the time step for pressure (and velocity) updates. We set the relation $\Delta t_p = C\Delta t_s$, where C is a positive integer, assuming that Δt_s is constant (in practice we allow for variable Δt_s). Therefore, pressure and velocity are updated at times $t_n = n\Delta t_p$, for $n = 0, 1, \ldots$, while the saturation is computed at intermediate times $t_{n,k} = t_n + k\Delta t_s$, for $k = 1, 2, \ldots, C$, such that $t_n < t_{n,k} \leq t_{n+1}$.

Accuracy can be further improved by extrapolation of the last computed velocities for each time $t_{n,k}$ of the saturation transport time step. In that sense, the velocity field to be considered at time $t_{n,k}$ can be computed as

$$\mathbf{u}^e(\mathbf{x}, t) = \begin{cases} \mathbf{u}^0(\mathbf{x}), & \text{if} \quad 0 \leq t \leq t_1, \\ \dfrac{t - t_{n-1}}{\Delta t_p}\,\mathbf{u}^n(\mathbf{x}) - \dfrac{t - t_n}{\Delta t_p}\,\mathbf{u}^{n-1}(\mathbf{x}), & \text{if} \quad t_n < t \leq t_{n+1}, \end{cases} \tag{4}$$

for each $t = t_{n,k}$, $k = 1, 2, \ldots, C$, where $\mathbf{u}^n(\mathbf{x})$ is the velocity computed by the pressure equation (1) at time $t = t_n$, approximating $\mathbf{u}(\mathbf{x}, t_n)$ (see [39]). The algorithm to compute the approximate solutions for saturation, velocity and pressure at time t_{n+1} from the solutions at time t_n, is described in Algorithm 1.

3.2. Solving the elliptic equation by the MRCM

Considering the most up-to-date saturation $s^{n+1}(\mathbf{x})$, one can obtain the most recent uniformly positive definite permeability tensor field $\kappa = \lambda(s^{n+1}(\mathbf{x}))K(\mathbf{x})$, which allows the solution of pressure equation in the whole domain Ω. The pressure equation (1) together with suitable boundary conditions can be written as

$$\begin{aligned} \mathbf{u} &= -\kappa \nabla p \quad \text{in } \Omega \\ \nabla \cdot \mathbf{u} &= q \quad \text{in } \Omega \\ p &= g \quad \text{on } \partial\Omega_p \\ \mathbf{u} \cdot \mathbf{n} &= z \quad \text{on } \partial\Omega_u \end{aligned} \tag{5}$$

Here, $q = q(\mathbf{x}, t)$ is a source term, $g = g(\mathbf{x}, t)$ the pressure boundary data and $z = z(\mathbf{x}, t)$ the normal velocity data ($\mathbf{n}$ is the outward unit normal), specified respectively at the boundaries $\partial\Omega_p$ and $\partial\Omega_u$. From now onwards, for the sake of notation, we will drop the time dependency on these equations, keeping in mind that this dependency can only come from the source term, the boundary data (which is rather uncommon in most applications), and most importantly, from the permeability field.

The Multiscale Robin Coupled method (MRCM) is a non-overlapping multiscale domain decomposition method that generalizes the Multiscale Mixed Method (MuMM) [19], which is based on a domain decomposition method that was first introduced by Douglas et al. [18]. The main idea of these methods is to subdivide the domain Ω in N non-overlapping subdomains Ω_i, $i = 1, 2, \ldots, N$, such that local solutions can be computed independently for each Ω_i (which is naturally parallelizable) in a fine scale h, associated to the size of the discretization of the local problems. Continuity of the solution is enforced by compatibility conditions, that in the multiscale sense, are weakly imposed only on a coarse scale $H \gg h$ to reduce computational cost. Let Γ be the skeleton of the decomposition, i.e., the union of all interfaces $\Gamma_{ij} = \Omega_i \cap \Omega_j$. This means that the multiscale solution $(\mathbf{u}_h, p_h)$ obtained by the MRCM satisfies the compatibility conditions

$$\int_\Gamma (\mathbf{u}_h^+ - \mathbf{u}_h^-) \cdot \check{\mathbf{n}}\, \psi \, d\Gamma = 0 \quad \text{and} \quad \int_\Gamma (p_h^+ - p_h^-)\, \phi \, d\Gamma = 0 \tag{6}$$

for all $(\phi, \psi) \in \mathcal{U}_H \times \mathcal{P}_H$, which are low-dimensional spaces defined over the set of edges $\mathcal{E}_h$ of the skeleton Γ. The $+$ and $-$ superscripts denote the solution on each side of the interface Γ. In this equation we refer to a fixed (global) normal vector $\check{\mathbf{n}}$ to the skeleton Γ, pointing outwards from the subdomain with smallest index. One of the key ingredients of the MRCM is the definition of normal flux and pressure unknowns at the interfaces, namely $(U_H, P_H) \in \mathcal{U}_H \times \mathcal{P}_H$ such that these compatibility conditions can be fulfilled by imposing the Robin-type boundary conditions on the local problems, namely

$$-\frac{\alpha H}{\kappa_i(\mathbf{x})}\, \mathbf{u}_h^i \cdot \check{\mathbf{n}}^i + p_h^i = -\frac{\alpha H}{\kappa_i(\mathbf{x})}\, U_H\, \check{\mathbf{n}} \cdot \check{\mathbf{n}}^i + P_H, \quad \mathbf{x} \in \Gamma_{ij}, \tag{7}$$

where $\Gamma_{ij} = \Omega_i \cap \Omega_j$ stands for the interfaces between Ω_i and its nearest neighbor subdomains Ω_j, $(\mathbf{u}_h^i, p_h^i)$ denotes the multiscale solution within subdomain Ω_i, and $\check{\mathbf{n}}^i$ is the normal vector to Γ pointing outwards of Ω_i.

Two observations can be drawn from equations (6)-(7). First one can note from (6) that in the limit case of $H = h$, the fine grid solution obtained in the undecomposed case is recovered, and continuity of both velocity and pressure is satisfied at the fine scale h. Second, the parameter appearing in equation (7) for the Robin boundary condition, namely

$$\beta_i(\mathbf{x}) = \frac{\alpha H}{\kappa_i(\mathbf{x})}, \tag{8}$$

can modify the behavior of the MRCM in such way that other popular methods can be recovered. It was demonstrated in [16] that in the limit $\alpha \to 0$, the solution of the Multiscale Mortar Mixed Finite Element Method (MMMFEM) of Arbogast et al. [20] is recovered, while in the limit $\alpha \to +\infty$, the solution of the Multiscale Hybrid-Mixed Finite Element Method (MHM) of Harder et al. [21,22] is obtained. This is intuitively controlled by the parameter α in equation (7): In the former (MMMFEM), only flux continuity is weakly imposed in the coarse scale, while in the latter (MHM), only pressure continuity is weakly imposed in the coarse scale. The choice of the coarse spaces $\mathcal{U}_H$ and $\mathcal{P}_H$ also plays an important role in the approximation, which is well explored in [17], however in this work we only consider low-dimensional polynomial spaces built as subspaces of

$$F_h(\mathcal{E}_h) = \{ f : \mathcal{E}_h \to \mathbb{R};\ f|_e \in \mathbb{P}_0\ ,\ \forall e \in \mathcal{E}_h \}\ . \tag{9}$$

The differential formulation of the MRCM can be written as: Find solutions $(\mathbf{u}_h^i, p_h^i)$ for each subdomain Ω_i, and global unknowns (U_H, P_H) satisfying the local problems

$$\begin{aligned} \mathbf{u}_h^i &= -\kappa\, \nabla p_h^i && \text{in } \Omega_i \\ \nabla \cdot \mathbf{u}_h^i &= q && \text{in } \Omega_i \\ p_h^i &= g_p && \text{on } \partial\Omega_i \cap \partial\Omega_p \\ \mathbf{u}_h^i \cdot \check{\mathbf{n}}^i &= g_u && \text{on } \partial\Omega_i \cap \partial\Omega_u \\ -\beta_i \mathbf{u}_h^i \cdot \check{\mathbf{n}}^i + p_h^i &= -\beta_i U_H \check{\mathbf{n}} \cdot \check{\mathbf{n}}^i + P_H && \text{on } \partial\Omega_i \cap \Gamma \end{aligned} \tag{10}$$

and the compatibility conditions on the skeleton Γ

$$\begin{aligned} \sum_{i=1}^{N} \int_{\partial\Omega_i\cap\Gamma} (\mathbf{u}_h^i \cdot \check{\mathbf{n}}^i)\, \psi \, d\Gamma &= 0 \\ \sum_{i=1}^{N} \int_{\partial\Omega_i\cap\Gamma} \beta_i (\mathbf{u}_h^i \cdot \check{\mathbf{n}}^i - U_H\, \check{\mathbf{n}} \cdot \check{\mathbf{n}}^i)\, \phi\, (\check{\mathbf{n}} \cdot \check{\mathbf{n}}^i)\, d\Gamma &= 0 \end{aligned} \tag{11}$$

which must hold for all pair of functions $(\phi, \psi) \in \mathcal{U}_H \times \mathcal{P}_H$. The complete variational formulation, some theoretical results about existence and uniqueness of the solution of MRCM, along with its implementation and algorithmic details can be seen in two previously published works [16,17], and will be omitted in this work for conciseness. In short, the efficient implementation of this method solves equations (10) in parallel to obtain a set of local multiscale basis functions, that are further used to write the global solution as a linear combination that is obtained by the solution of the global problem induced by equation (11).

Notice that no method was specified for the discretization of (10). Any method such as finite volumes, finite elements or finite differences can be used, provided that edge fluxes and pressures at subdomain interfaces are available for the multiscale method when requested.

We intend to take advantage of the flexibility of the MRCM to improve its accuracy by introducing an adaptive strategy to select the regions of high permeability for a specific treatment. For this purpose, instead of dealing with a previously fixed α parameter in equation (8), we will instead consider a more flexible definition of β_i,

$$\beta_i(\mathbf{x}) = \frac{\alpha(\mathbf{x}) H}{\kappa_i(\mathbf{x})}, \tag{12}$$

such that $\alpha(\mathbf{x})$ can be locally chosen in an adaptive fashion.

3.3. Cost estimation of the MRCM

The overall cost of the MRCM method can be assessed in previous publications (see [16,17]). To give an idea of the cost of just the elliptic solver by the MRCM in 2D, suppose we have a domain decomposition of $N = N_x \times N_y$ subdomains, each one with $n_x \times n_y$ fine grid cells. The cost is heavily dependent on the choice of the interface spaces $\mathcal{U}_H$ and $\mathcal{P}_H$, described above. Let $N_U = \dim(\mathcal{U}_H)$ and $N_P = \dim(\mathcal{P}_H)$ be the dimensions of the interface spaces, the number of multiscale basis functions in each subdomain can be estimated as $N_B = 4 \times (N_U + N_P) + 1$, which corresponds to the set of homogeneous basis functions for each one of the 4 edges of the subdomain, plus one additional basis function for the inhomogeneous part of the solution. Notice that some subdomains will have less than that due to physical boundary conditions. To compute the complete set of multiscale basis functions, one has to solve approximately N_B problems for a grid size of $n_x \times n_y$ cells per each one of the N subdomains. These problems are independent and can be solved in parallel using multicore machines.

To complete the MRCM algorithm, the solution of one global problem (11) has to be computed to write the final solution. The size of this global problem depends on the number of interfaces between subdomains, that is exactly $N_I = N_x \times (N_y - 1) + N_y \times (N_x - 1)$. Then the size of the global interface system is estimated to be $N_I \times (N_U + N_P)$.

Let us consider as an example a domain decomposition of 11×3 subdomains discretized by 20×20 fine grid cells each, with linear interface spaces for both flux and pressure. This is a typical domain decomposition in the numerical experiments below. In this example, $N_U = N_P = 2$, and the total number of multiscale basis functions to be computed is roughly $N_B = 17$ per subdomain, requiring the solution of linear systems for a grid size of $20 \times 20 = 400$ cells. The total amount of work is thus (a) solving 33 local linear systems of dimension 400, each with 17 different right-hand sides, which can be solved all in parallel with no required communication between processing cores, plus (b) solving the global system (11) that couples the different subdomains, which has size $N_I \times (N_U + N_P) = 52 \times 4 = 208$ unknowns. Therefore the solution yielded by the MRCM for this example, computed in a parallel environment, is, in principle, cheaper than the cost of the undecomposed case, which requires the solution of a linear system for a grid of size $220 \times 60 = 13200$ cells. The gain increases when larger, three-dimensional problems are considered.

3.4. Velocity post-processing (downscaling)

The weak imposition of flux continuity in a coarse scale by the MRCM brings a well known problem in multiscale methods: the normal component of fluxes may not be continuous at the interfaces of the skeleton Γ. A continuous flux at the fine scale is necessary for applications involving the transport of species, such as pollutants (in single-phase flows) or saturation (in two-phase flows and more complex models). Solutions for this problem include post-processing fluxes using downscaling techniques [48,19,2].

One of these possible approaches is by averaging fluxes on interfaces defined by

$$\bar{\mathbf{u}}_h^{ij} = \frac{1}{2}\left(\mathbf{u}_h^i|_{\Gamma_{ij}} + \mathbf{u}_h^j|_{\Gamma_{ij}}\right), \tag{13}$$

for each interface Γ_{ij}, which defines a unique normal flux, but unbalances masses across subdomains. A remedy is to use the averaged fluxes at the interfaces to define new Neumann local problems to recover mass conservation at the fine scale, by solving

$$\begin{aligned} \nabla \cdot \tilde{\mathbf{u}}_h^i &= q^i && \text{in } \Omega_i \\ \tilde{\mathbf{u}}_h^i &= -\kappa\, \nabla \tilde{p}_h^i && \text{in } \Omega_i \\ \tilde{\mathbf{u}}_h^i \cdot \check{\mathbf{n}}^i &= \mathbf{u}_h^i \cdot \check{\mathbf{n}}^i && \text{on } \partial\Omega_i \cap \partial\Omega \\ \tilde{\mathbf{u}}_h^i \cdot \check{\mathbf{n}}^i &= \bar{\mathbf{U}}_h^{ij} \cdot \check{\mathbf{n}}^i && \text{on } \Gamma_{ij}\ \forall j \end{aligned} \tag{14}$$

for all Ω_i, $i = 1, 2, \ldots, N$. Note that the local problems are undefined up to a pressure constant. In order to remove this indeterminacy, a common approach is to impose pressure at some point. After solving all these local problems, normal fluxes are ensured to be continuous and the overall solution is conservative, however, by doing that we violate Darcy's law across subdomains, which is a small price to pay for normal flux continuity. The cost of the downscaling post-processing is one extra local problem solution per subdomain.

4. Numerical results

In this section we present numerical experiments to investigate the accuracy of the MRCM in the approximation of two-phase flows in high-contrast permeability fields typical of petroleum reservoirs. Initially we study global errors of saturation and velocity fields and compare our findings with single-phase flows results discussed in [16,17]. Then we focus on a detailed analysis of fingering instabilities in heterogeneous permeability fields. Initially we consider high-contrast permeability fields having either a high permeability channel or a low permeability region. Our numerical studies indicate that the best solutions for two-phase flows in such challenging fields occur for extreme values of α. These numerical results will be used in the design of an adaptive strategy for setting the parameter α, aiming at an improved accuracy of the MRCM solution.

In all simulations the reservoir is initially fully saturated with oil and water is injected at a constant rate. We use quadratic relative permeability curves: $k_{ro} = (1-s)^2$ and $k_{rw} = s^2$, such that the fractional flow function is given by

$$f(s) = \frac{Ms^2}{Ms^2 + (1-s)^2}, \tag{15}$$

where $M = \mu_o/\mu_w$. We take $M = 40$ in our numerical experiments.

For each production well the oil fractional flow $\mathcal{F}(t)$ (the fraction of oil in the produced fluid) is given by

$$\mathcal{F}(t) = 1 - \frac{\int_{\partial\Omega_{\text{out}}} f(s)\, \mathbf{u}\cdot\mathbf{n}\, dl}{\int_{\partial\Omega_{\text{out}}} \mathbf{u}\cdot\mathbf{n}\, dl}, \tag{16}$$

where $\partial\Omega_{\text{out}}$ denotes the outflow well boundaries with the outward unit normal $\mathbf{n}$. We refer to the dimensionless time expressed in PVI (pore volume injected), a standard time unit in reservoir simulation that refers to the fraction of the total accessible pore volume that has been injected into the domain [49]

$$T_{\text{PVI}} = -V_p^{-1} \int_0^t \int_{\partial\Omega_{\text{in}}} \mathbf{u}(\mathbf{x},\tau)\cdot\mathbf{n}\, dl\, d\tau, \tag{17}$$

where V_p is the total pore-volume of the reservoir, t is the time taken for injection and $\partial\Omega_{\text{in}}$ the inflow well boundaries with the outward unit normal $\mathbf{n}$.

The time steps are chosen such that they satisfy a CFL condition [50]. The number of transport steps between successive elliptic updates used in the operator splitting scheme is at most 20.

We present and discuss results of numerical simulations performed with two-dimensional permeability fields set initially to be layers of the 3D SPE10 field (http://www.spe.org/web/csp/index.html) [51]. For the fields considered here the permeability contrast is $K_{\max}/K_{\min} \approx 10^6$ and the computational grid has 220×60 cells distributed on a rectangular domain $\Omega = [0, 11/3] \times [0, 1]$. In most of our simulations, we consider a slab geometry, with no-flow boundary conditions at the top and bottom boundaries ($y = 0$ and $y = 1$) along with an imposed flux on the left ($x = 0$) and right ($x = 11/3$) boundaries, with no source terms. This is the geometry considered in the numerical experiments unless stated otherwise.

Concerning the MRCM, we consider linear spaces $\mathcal{P}_{H,1}$ and $\mathcal{U}_{H,1}$ for interfaces unknowns. For simplicity, the skeleton partition $\mathcal{T}_H$ is built by taking only one element per interface Γ_{ij} between subdomains. Refinements of $\mathcal{T}_H$ are possible in the MRCM algorithm, but these are left for future work.

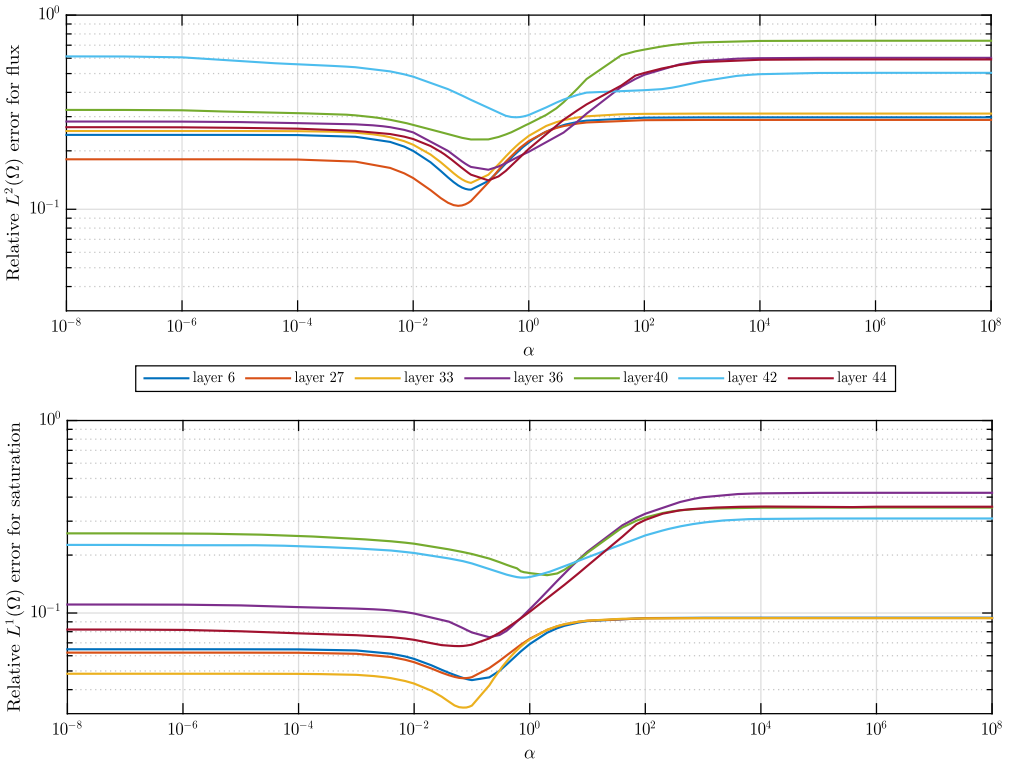

Fig. 1. Relative errors computed at $T_{\text{PVI}} = 0.3$. $L^2(\Omega)$ errors for flux (top) and $L^1(\Omega)$ errors for saturation (bottom). Each curve shows the results of a different SPE10 layer as a function of the algorithmic parameter α. Note that the minimum errors for saturation and flux are attained at intermediate values of α. (For interpretation of the colors in the figure(s), the reader is referred to the web version of this article.)

4.1. Two-phase flows: global errors

The objective of this study is to investigate whether the improved accuracy shown by the MRCM when compared to existing procedures in the approximation of single phase flow [16,17] is also present for two-phase flows. In the references just mentioned the improved accuracy of the MRCM indicates that typically minimal error for pressure and flux is attained somewhere between the MMMFEM-like and MHM-like solutions. Note that by setting small (respectively, large) values for the MRCM algorithmic parameter α one can produce MMMFEM-like (resp., MHM-like) numerical approximations.

Numerical results obtained with the MRCM for two-phase problem at $T_{\text{PVI}} = 0.3$ are shown in Fig. 1 for some selected layers of the SPE10 field that contain channelized structures. The domain is divided into 11×3 subdomains with 20×20 cells into each one. The $L^2(\Omega)$ and $L^1(\Omega)$ relative errors, for flux and water saturation, respectively, are computed with respect to a reference fine grid solution. Fig. 1 shows that the behavior of the errors for the flux is similar to that reported in [16], where a strong dependence on the parameter α is noticed. We have observed that applying a downscaling procedure (used here, but not in [16]) shifts the position of the minimum for the errors from values of $\alpha \in [1, 100]$ to $\alpha \in [0.01, 1]$. Moreover, the minimum errors for saturation and flux are attained at essentially the same values of α. Once the minimum errors for saturation occur for intermediate values of α we confirm that the MRCM when applied to two-phase flows produces more accurate solutions when compared to both MMMFEM and MHM. We have selected layer number 36 of the SPE10 field to investigate flux and saturation errors throughout a simulation. Fig. 2 shows that the minima for both quantities do not vary significantly over time.

Next, in line with similar studies discussed in [1,17], we consider all SPE10 layers in a study to assess the accuracy of the MRCM when compared to two-phase flows approximated by the MMMFEM and the MHM. We set $\alpha = 1$ in the MRCM (see [17] for a justification of this choice) and we refer to the method with this choice as the MRCM-usual. In order to produce MMMFEM-like and MHM-like solutions we take $\alpha = 10^{-8}$ and $\alpha = 10^{8}$, respectively. In Fig. 3 we present $L^2(\Omega)$ and $L^1(\Omega)$ relative errors for flux and saturation, respectively. The errors are computed at $T_{\text{PVI}} = 0.3$ for all SPE10 layers. Note that the MHM-like solutions are the least accurate ones, a result that is similar to a study presented in [17] (performed with other choices of interface spaces, without the effect of downscaling and for single-phase flows). The MRCM-usual solution is comparable in accuracy to the MMMFEM-like solution, however for the flux variable the MMMFEM-like solution behaves poorly for some of the layers around 40 and 80. These results are reflected also in the corresponding saturation fields. Our results indicate that the MRCM-usual produces more accurate solutions for flux and saturation than the corresponding solutions produced with the MHM-like method, for all layers of the SPE10 field. Moreover the MRCM-usual results are more

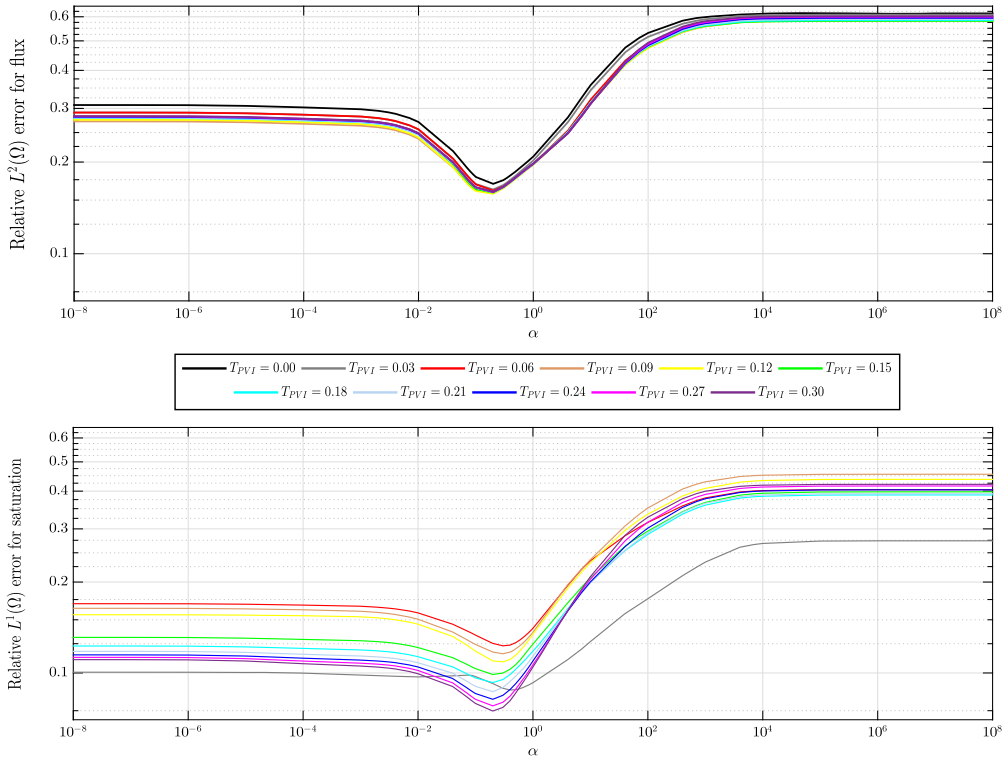

Fig. 2. Relative errors for layer 36 as a function of the algorithmic parameter α at different times. $L^2(\Omega)$ errors for flux (top) and $L^1(\Omega)$ errors for saturation (bottom). Note that the behavior of errors for both quantities do not vary significantly throughout the simulation.

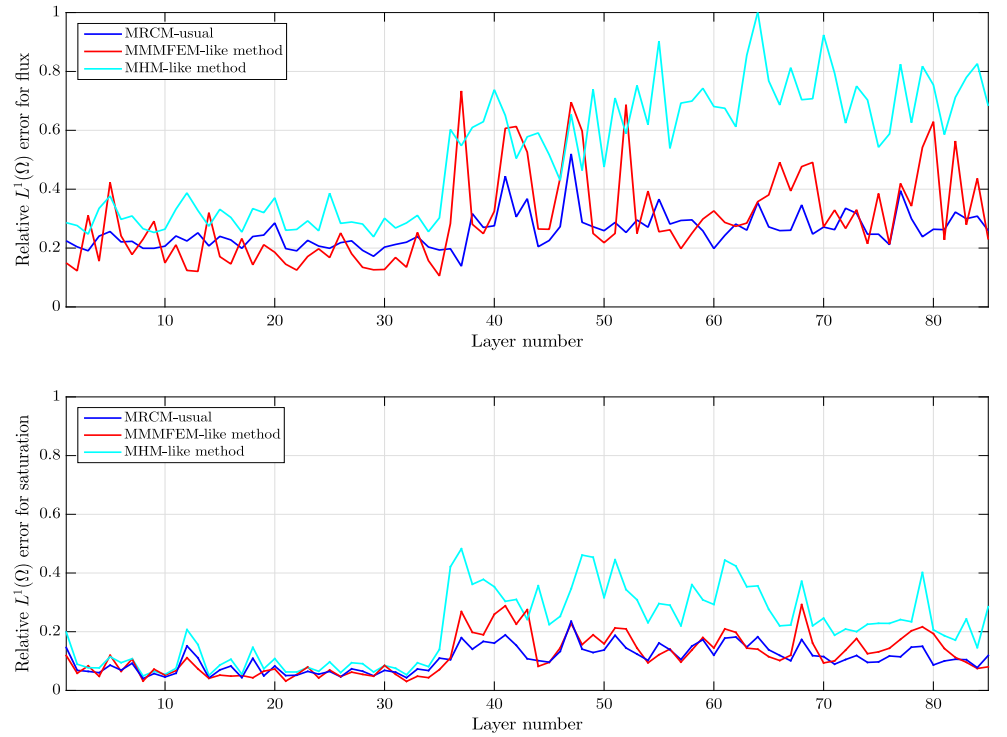

Fig. 3. Relative flux and saturation errors for the MRCM-usual, the MMMFEM-like method and the MHM-like method for each layer of the SPE10 field at $T_{\text{PVI}} = 0.3$. $L^2(\Omega)$ error for flux (top) and $L^1(\Omega)$ error for saturation (bottom). Note that the MRCM-usual is the most accurate procedure on highly channelized permeability layers (36 to 85).

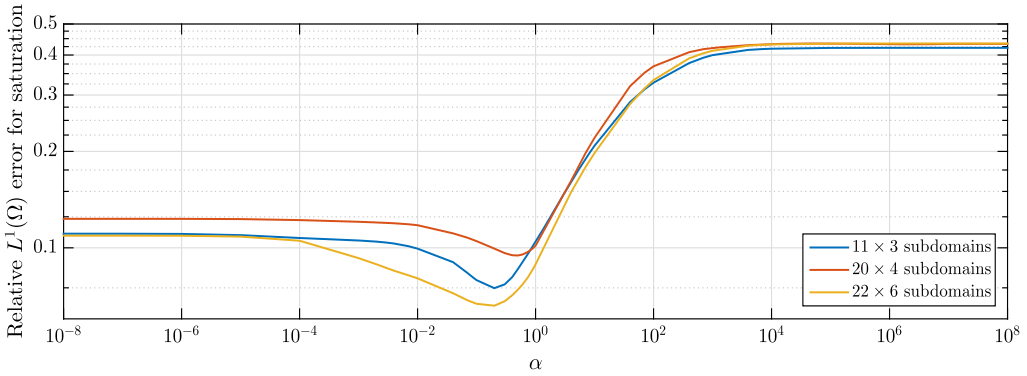

Fig. 4. Relative $L^1(\Omega)$ error for saturation as a function of the algorithmic parameter α for different choices of the domain decomposition. Errors are calculated for the 36th layer of the SPE10 field at $T_{\text{PVI}} = 0.3$. We compare results for subdivisions of the domain in 11×3, 20×4 and 22×6 subdomains with 20×20, 11×15 and 10×10 fine grid cells in each subdomain, respectively. Note that all domain decompositions considered share the same trend for the saturation error curves.

accurate than the simulation results performed with the MMMFEM-like method in the case where the permeability field is highly channelized (layers 36 to 85).

We close this discussion of global errors with the result reported in Fig. 4. In order to illustrate that the choice of a domain decomposition does not affect the main trend of saturation error curves, we consider different domain decompositions for the 36th layer of SPE10 project. Errors are computed at $T_{\text{PVI}} = 0.3$ and can be seen in Fig. 4. We consider subdivisions of 11×3, 20×4 and 22×6 subdomains, having 20×20, 11×15 and 10×10 fine grid cells inside each subdomain, respectively.

Multi-phase flows in high-contrast formations are typically dominated by fingering instabilities. The details of such fingers are not well captured by the global norms considered above. However, the correct approximations of such water-oil fingers is essential in predicting breakthrough times, that are important for decision making in reservoir engineering. Next we perform a more detailed assessment of the performance of multiscale mixed methods by comparing their 2D saturation profiles. We will also compare results produced by multiscale mixed methods with a classical multiscale method: the Multiscale Finite Volume Method (MSFV) [2,52].

4.2. Two-phase flows: detailed analysis

We now compare saturation profiles of two-phase flows approximated by the MRCM, the MMMFEM-like and MHM-like procedures and the MSFV.

4.2.1. Permeability field with a high permeability channel

In our first study we consider the 36th layer of the SPE10 field with a domain decomposition of 20×4 subdomains, each one discretized by 11×15 cells. Note that the MSFV version that we use for comparison (presented in [2] with the correction functions proposed in [52]) requires an odd number of cells in each direction in the discretization of subdomains. Layer 36 of the SPE10 project has a channel of high permeability. The approximation of the velocity field in such a high-contrast formation presents a challenge for the multiscale methods. Fig. 5 shows the permeability field (log-scaled) along with the saturation profiles at $T_{\text{PVI}} = 0.06$ (before breakthrough time) approximated by multiscale methods. The methods that produce a saturation solution closer to the reference run (fine grid solution of the problem at hand) are the MRCM-usual and MMMFEM-like method, while the latter is the most accurate in capturing the details of the fingers. The MSFV and the MHM-like method produce very inaccurate solutions for this channelized permeability field. The oil production curves along with saturation relative errors corresponding to the simulations reported in Fig. 5 are displayed in Fig. 6. In this figure, the breakthrough time for the fine grid simulation is illustrated by a dashed line in the saturation relative errors plot. The oil production curve computed by the MHM-like method clearly differs considerably from the reference one. The procedures that better predict oil production curves are the MRCM-usual and the MMMFEM-like method. The saturation global errors reflect these results: we note that the errors associated with the MRCM-usual and MMMFEM-like method are the smallest.

We also consider another version of this example by using a point source for water injection and production wells, along with no-flow boundary condition in the whole domain, keeping the same permeability field and domain decomposition of the previous case. Water is injected at the bottom-left corner while the production well is located at the top-right corner. The saturation profiles at $T_{\text{PVI}} = 0.13$ (just before breakthrough time) are shown in Fig. 7, where one can observe the same behavior as for the slab geometry, with the MMMFEM-like being the most accurate in capturing the details of the fingers. Similar results are also attained for the oil production curves and saturation relative errors, presented in Fig. 8, where better predictions of oil production curves are obtained by the MMMFEM-like method, as well as the smallest saturation global errors.

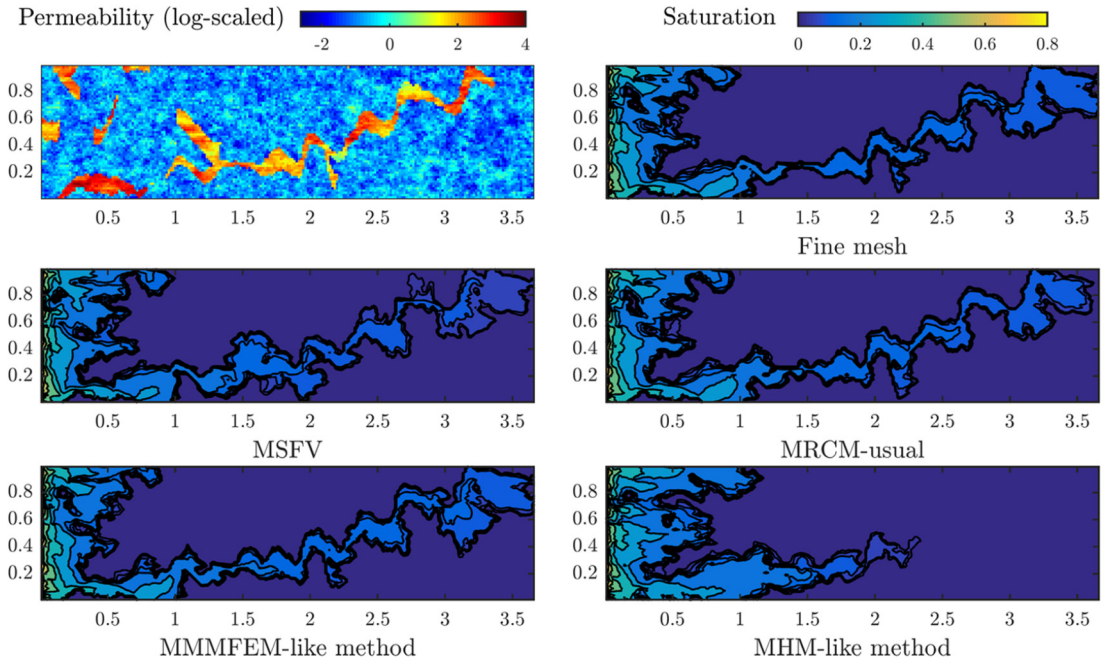

Fig. 5. Comparison of multiscale methods. Saturation profiles at $T_{\text{PVI}} = 0.06$ for layer 36 of the SPE10 field are shown. Left column, top to bottom: high-contrast permeability field (log-scaled); MSFV saturation profile; MMMFEM-like saturation profile. Right column, top to bottom: reference fine grid solution; MRCM-usual saturation profile; MHM-like saturation profile. The MMMFEM-like method is the most accurate in capturing the details of the fingers on this field with a high permeability channel.

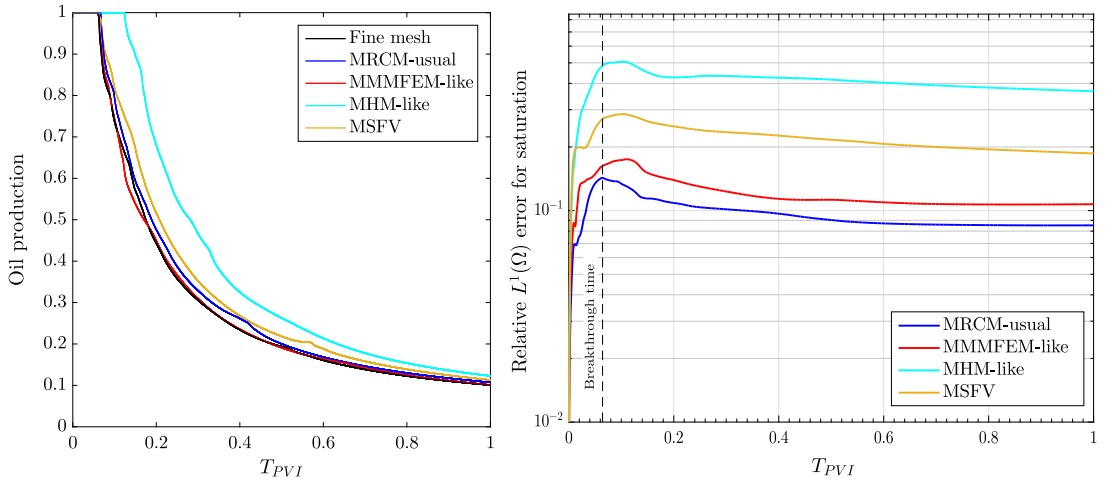

Fig. 6. Oil production curve (left) and relative $L^1(\Omega)$ errors for saturation (right) on layer 36 of SPE10 model as a function of time. The breakthrough time is illustrated by a dashed line (right plot). We note that the best approximations of oil production curves and the smallest saturation errors are performed by the MRCM-usual and MMMFEM-like method.

4.2.2. Permeability field with a region of low permeability

Regions of low permeability also pose difficulties for multiscale methods. In order to assess the various methods considered here in such a situation we built a region of low permeability taking advantage of the channelized structure of layer 36. We consider a region at the bottom left corner of the layer 36 with 165×45 fine grid cells divided into 15×3 subdomains. The low permeability region is defined along the channel of layer 36. The boundary conditions for this case follow the slab geometry as before. Fig. 9 shows the permeability field (log-scaled) with the region of low permeability and saturation profiles at $T_{\text{PVI}} = 0.09$ (before breakthrough). In contrast to our findings in the previous example the only procedure that produces a saturation field close to the reference solution is the MHM-like method. Fig. 10 shows the oil production curve and the relative saturation error as a function of time. Note that all oil production curves are quite inaccurate. This confirms that problems with obstacles are difficult to approximate by multiscale methods. The saturation

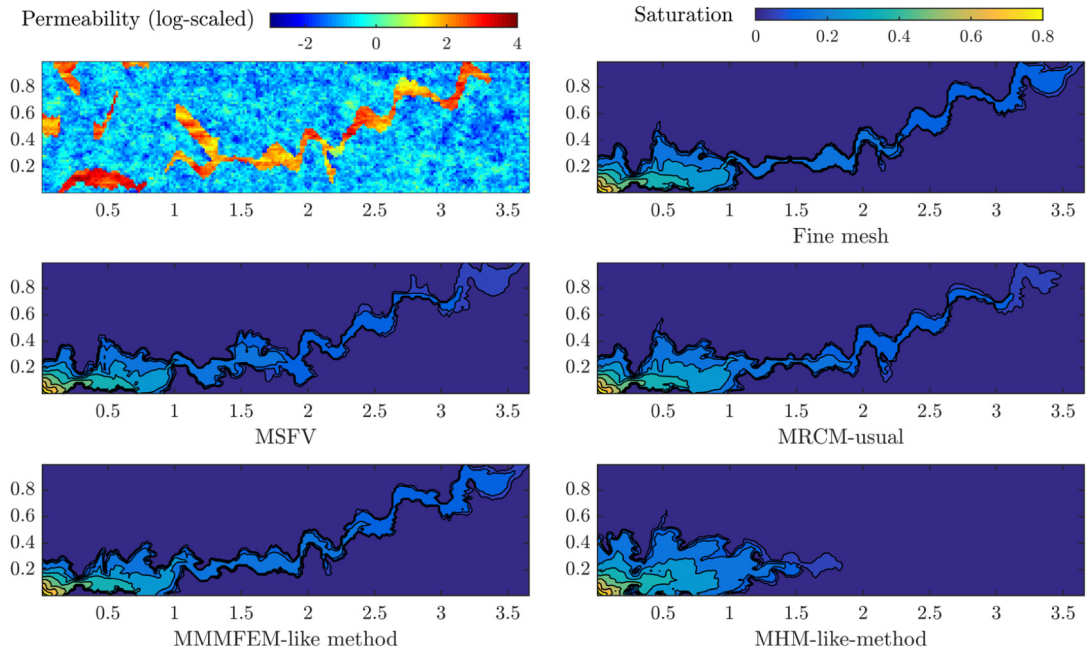

Fig. 7. Comparison of multiscale methods using point source and no-flow boundary conditions. Saturation profiles at $T_{\text{PVI}} = 0.13$ for layer 36 of the SPE10 field are shown. Left column, top to bottom: high-contrast permeability field (log-scaled); MSFV saturation profile; MMMFEM-like saturation profile. Right column, top to bottom: reference fine grid solution; MRCM-usual saturation profile; MHM-like saturation profile. The MMMFEM-like method is the most accurate in capturing the details of the fingers.

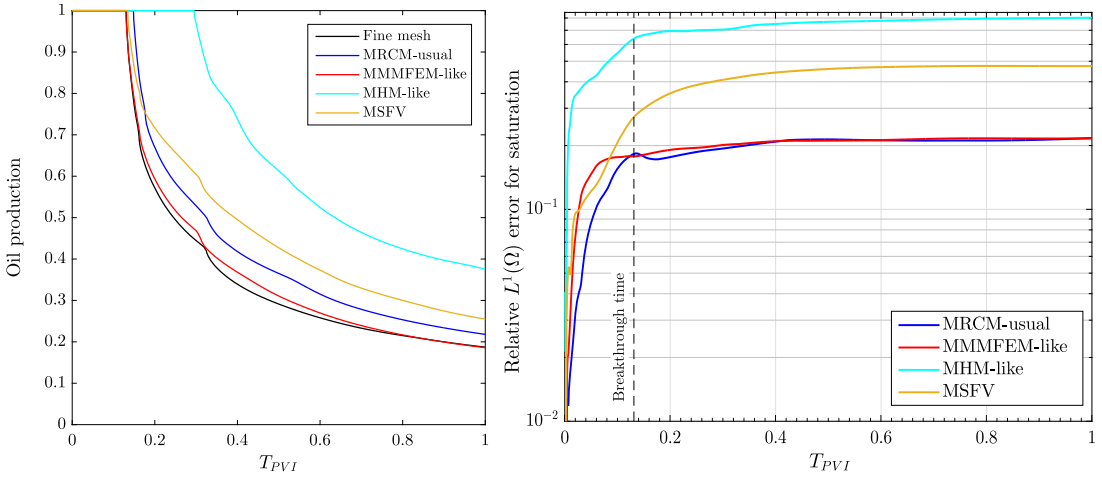

Fig. 8. Oil production curve (left) and relative $L^1(\Omega)$ errors for saturation (right) on layer 36 of SPE10 model as a function of time using point source and no-flow boundary conditions. The breakthrough time is illustrated by a dashed line (right plot). We confirm the better performance of the MMMFEM-like method throughout the simulation.

errors produced by the MHM-like method after breakthrough time are the smallest. These results indicate that the remaining procedures (MRCM, MMMFEM-like method and MSFV) produce poor quality solutions in presence of low permeability regions.

We repeat this example now with point source and sink, along with no-flow boundary condition in the whole domain, keeping the same permeability field and domain decomposition as the previous simulation. Water is injected at the bottom-left corner, while the production well is located at the top-right corner of the domain. The saturation profiles at $T_{\text{PVI}} = 0.18$ (just before breakthrough time) are shown in Fig. 11, where one can note that the MHM-like is the most accurate method, the same conclusion as in the slab geometry case. Similar results are also obtained for the oil production curves and saturation relative errors, which are presented in Fig. 12. All approximations of oil production curves are inaccurate and the smallest saturation global errors after breakthrough time are associated with the MHM-like method.

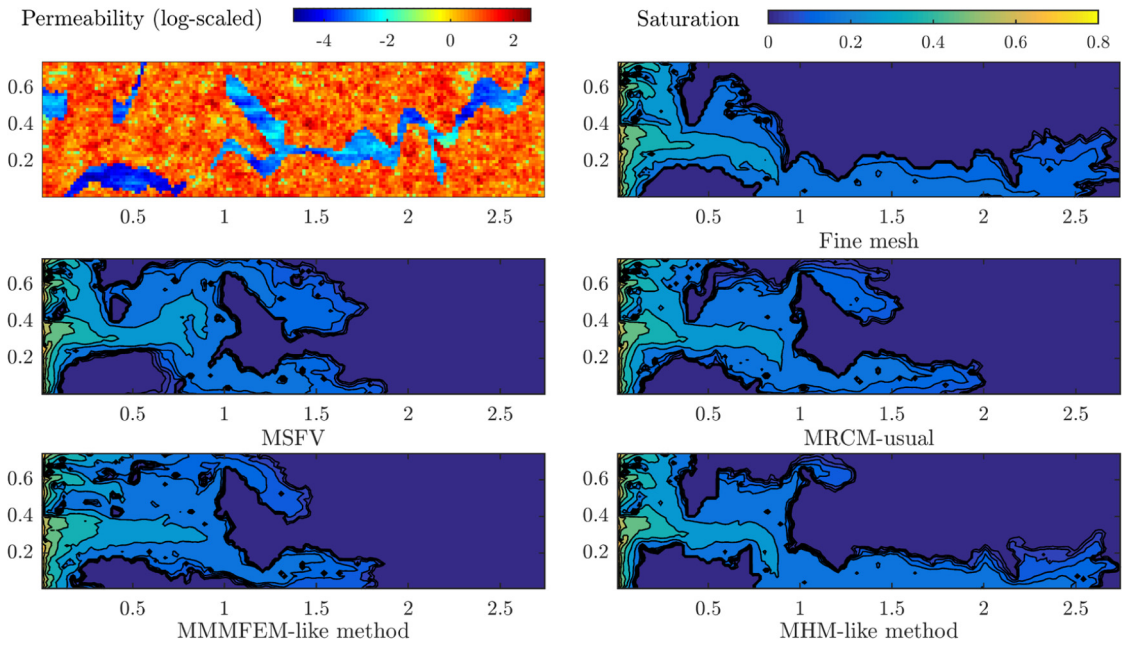

Fig. 9. Comparison of multiscale methods. Saturation profiles at $T_{\text{PVI}} = 0.09$ for a permeability field exhibiting a low permeability region are shown. Left column, top to bottom: high-contrast permeability field (log-scaled); MSFV saturation profile; MMMFEM-like saturation profile. Right column, top to bottom: reference fine grid solution; MRCM-usual saturation profile; MHM-like saturation profile. Note that the MHM-like solution is considerably more accurate than the others.

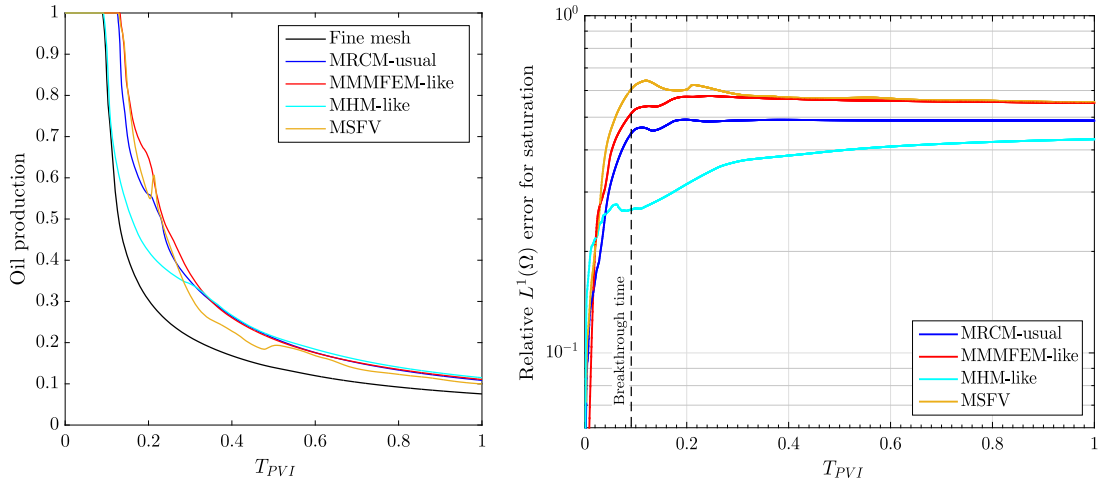

Fig. 10. Oil production curve (left) and relative $L^1(\Omega)$ errors for saturation (right) on a region of low permeability as function of time. The breakthrough time is illustrated by dashed line (right plot). We note that all approximations of oil production curves are inaccurate. The smallest saturation errors are obtained by the MHM-like method.

4.3. Adaptive MRCM

The two studies reported above (permeability fields with either a high permeability channel and a low permeability region) illustrate the difficulties of multiscale methods in the approximation of velocity fields in high-contrast formations. Although relative errors for saturation attain minima for the MRCM with the algorithmic parameter $\alpha \approx 1$ (see Fig. 1) we have determined that $\alpha = 10^{-8}$ (the MMMFEM-like method) is appropriate for the approximation of velocity fields in the presence of high-permeability channels. This is an indication that the coupling of nearest neighbor subdomains through the imposition of a continuous pressure is the best strategy to approximate flow in the presence of high permeability channels. On the other hand, the coupling of subdomains through the imposition of continuous normal components of fluxes accomplished by setting $\alpha = 10^{8}$ (the MHM-like method) is an adequate strategy to handle low permeability regions. Note that the MRCM, as opposed to the other multiscale procedures discussed here, has enough built-in flexibility to handle both challenging permeability fields, by varying its algorithmic parameter α.

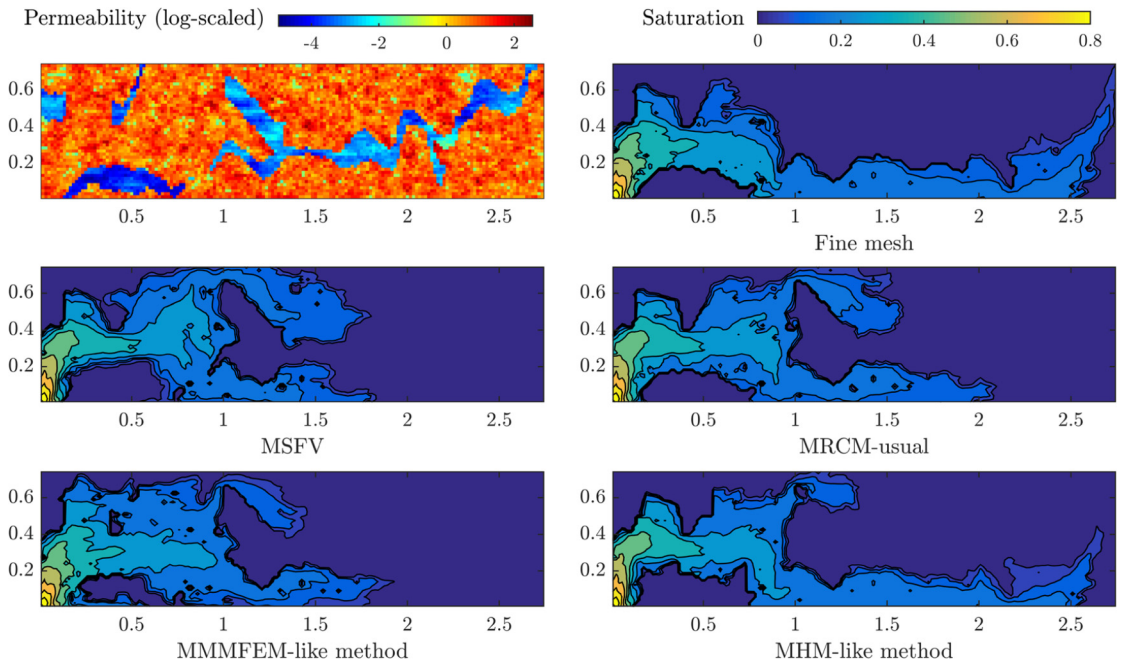

Fig. 11. Comparison of multiscale methods using point source and no-flow boundary conditions. Saturation profiles at $T_{\text{PVI}} = 0.18$ for a permeability field exhibiting a low permeability region are shown. Left column, top to bottom: high-contrast permeability field (log-scaled); MSFV saturation profile; MMMFEM-like saturation profile. Right column, top to bottom: reference fine grid solution; MRCM-usual saturation profile; MHM-like saturation profile. Note that the MHM-like solution is the most accurate.

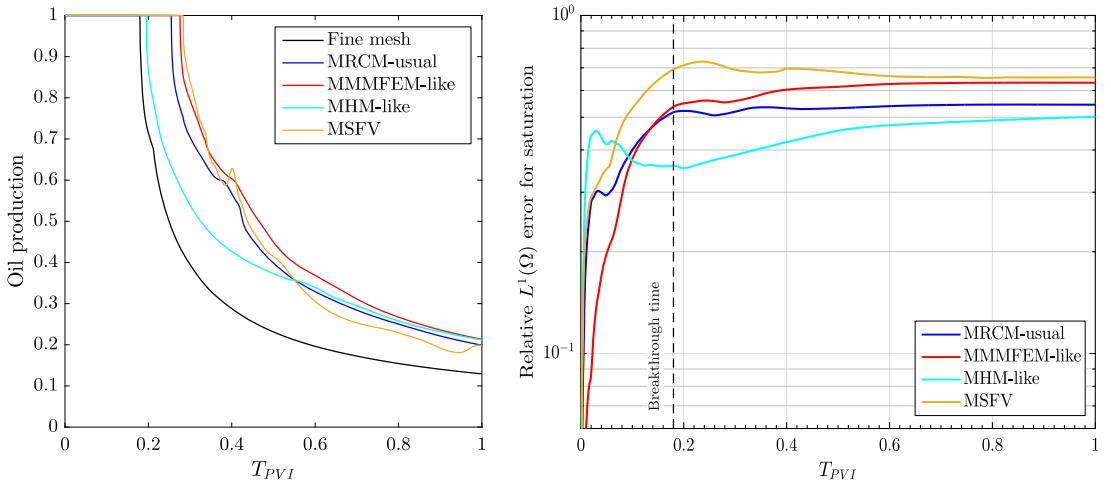

Fig. 12. Oil production curve (left) and relative $L^1(\Omega)$ errors for saturation (right) on a region of low permeability as a function of time, using point source and no-flow boundary conditions. The breakthrough time is illustrated by a dashed line (right plot). We confirm the better performance of the MHM-like method.

In order to further assess the accuracy of the methods considered here we construct a challenging, high-contrast permeability field that contains both types of structures: a high permeability channel and a low permeability region. The domain considered is $\Omega = [0, 33/12] \times [0, 3/2]$ with 165×90 fine grid cells equally divided into 15×6 subdomains. The upper half of the permeability field contains part of the channel structure from layer 36 of the SPE10 project and the lower half contains a region of low permeability. The permeability contrast is $K_{\max}/K_{\min} \approx 10^9$ and the field is shown in Fig. 13. The upper and lower regions are separated by a low permeability strip. The studies reported above indicate that for this permeability field all the multiscale methods that we have considered might produce inaccurate solutions.

In order to approximate the saturation solution in this challenging permeability field we propose initially a naive strategy for the selection of the MRCM parameter α. We use $\alpha = 10^{-8}$ (MMMFEM-like method) for the upper half containing the high permeability channel and $\alpha = 10^{8}$ (MHM-like method) for the half containing the low permeability region. We refer to this method as the MRCM-naive. We intend to use this example as a proof of concept: by varying the algorithmic parameter

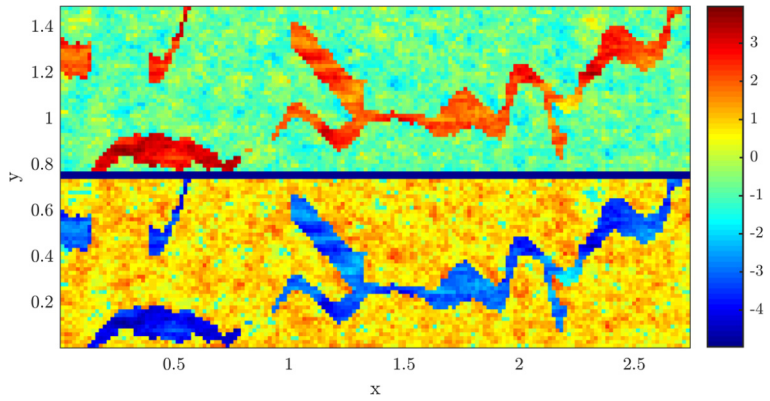

Fig. 13. A high-contrast permeability field (log-scaled) built to assess the accuracy of multiscale methods. The upper half contains the channel structure from layer 36 of the SPE10 field and the lower half contains a low permeability region. The permeability contrast is $K_{\max}/K_{\min} \approx 10^9$.

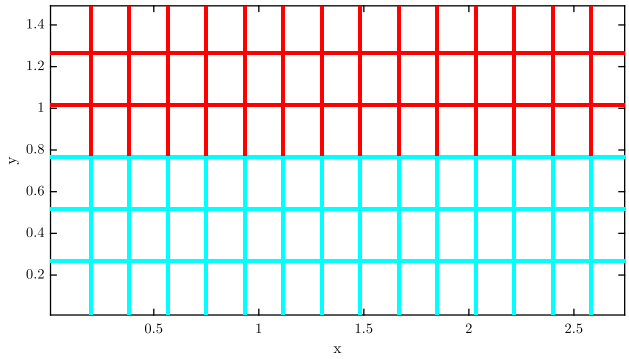

Fig. 14. Choice of the parameter α on subdomain boundaries for the MRCM-naive. The upper half considers the MMMFEM-like method by setting $\alpha = 10^{-8}$ (red). The lower half considers the MHM-like method by setting $\alpha = 10^8$ (cyan).

α of the MRCM we intend to show that we can produce good approximations velocity fields in complex, high-contrast formations. Clearly this strategy would not be applicable in fields exhibiting multiple channelized and low permeability regions. We will address the general case later.

Fig. 14 shows the choice for α at the boundaries of subdomains. A comparison of multiscale solution methods at $T_{\text{PVI}} = 0.06$ is illustrated in Fig. 15. For the upper half of the domain the MHM-like procedure is clearly inaccurate while for the lower half the remaining procedures (MSFV, MRCM-usual and the MMMFEM-like method) provide poor approximations. Therefore the only procedure that produces a saturation solution close to the reference run is the MRCM-naive. Fig. 16 shows the comparison of saturation profiles at $T_{\text{PVI}} = 0.5$, where it can be seen that these findings are even more evident after breakthrough.

Aiming at approximating velocity fields in realistic permeability fields where a clear separation of high and low permeability regions would not be possible we introduce an adaptive strategy for the choice of the α parameter. The basic idea is to identify the regions of high permeability and set α adaptively. We remark that a special treatment for distinct permeability regions has recently appeared in [6] where the focus was the construction of additional multiscale basis functions in selected regions. Our focus is computationally more competitive because we achieved improved approximation capabilities without adding multiscale basis function to the original set.

Our proposed strategy consists in setting the value of α locally, depending on the values of the permeability field at the boundaries of the subdomains. We set $\alpha = 10^{-8}$ (a MMMFEM-like method) for regions where the permeability is larger than a cutoff value ζ and $\alpha = 10^8$ (a MHM-like method) for the remaining subdomain boundaries. This procedure can be considered in a preprocessing operation, in which we map the absolute permeability variations and set α only once in an offline step. We refer to MRCM with α set through this procedure as the MRCM-adaptive. Fig. 17 shows the α values set by the proposed method for $\zeta \in [10^0, 10^1, 10^2, 10^3]$. We note that the high permeability channel structure is well captured for $\zeta = 10^1$ or $\zeta = 10^2$. In the study reported below we set $\zeta = 10$.

The comparison of saturation profiles for the MRCM (MRCM-usual, MRCM-naive and MRCM-adaptive) at $T_{\text{PVI}} = 0.06$ is displayed in Fig. 18. Note in Fig. 18 that the MRCM-naive and MRCM-adaptive provide more accurate solutions than the MRCM-usual. This comparison for a later time ($T_{\text{PVI}} = 0.5$) is shown in Fig. 19. Note that the better solutions produced by the MRCM-naive and MRCM-adaptive remain the best after breakthrough. Fig. 20 shows oil production curves and relative saturation errors as a function of time. The procedures that yield oil production curves close to the reference one are

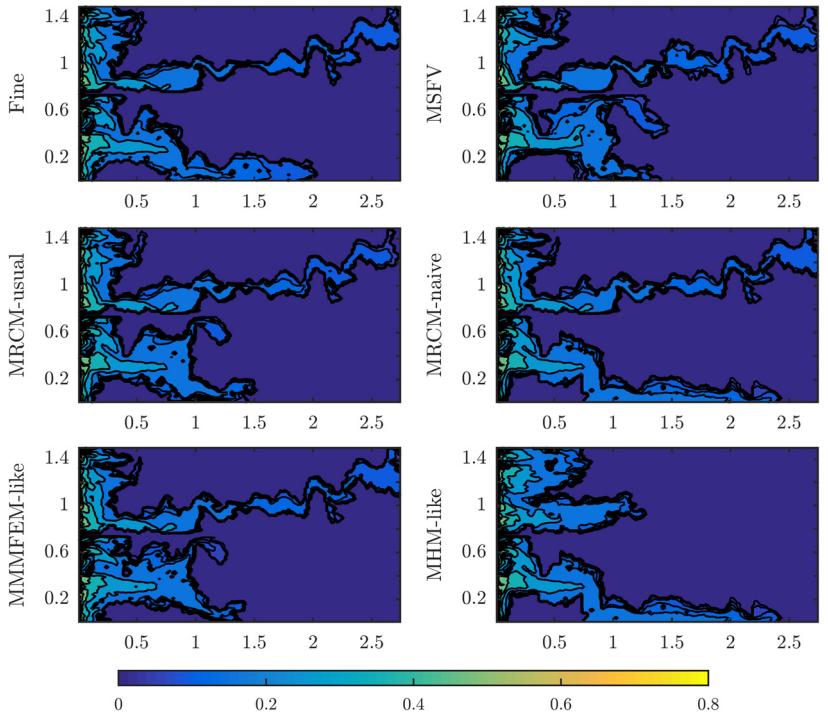

Fig. 15. Saturation profiles at $T_{\text{PVI}} = 0.06$ (before breakthrough) on the high-contrast permeability field that combines a high permeability channel and a low permeability region. Left column, top to bottom: reference fine grid solution; MRCM-usual saturation profile; MMMFEM-like saturation profile. Right column, top to bottom: MSFV saturation profile; MRCM-naive saturation profile; MHM-like saturation profile. The only procedure that produces a saturation solution close to the reference run is the MRCM-naive.

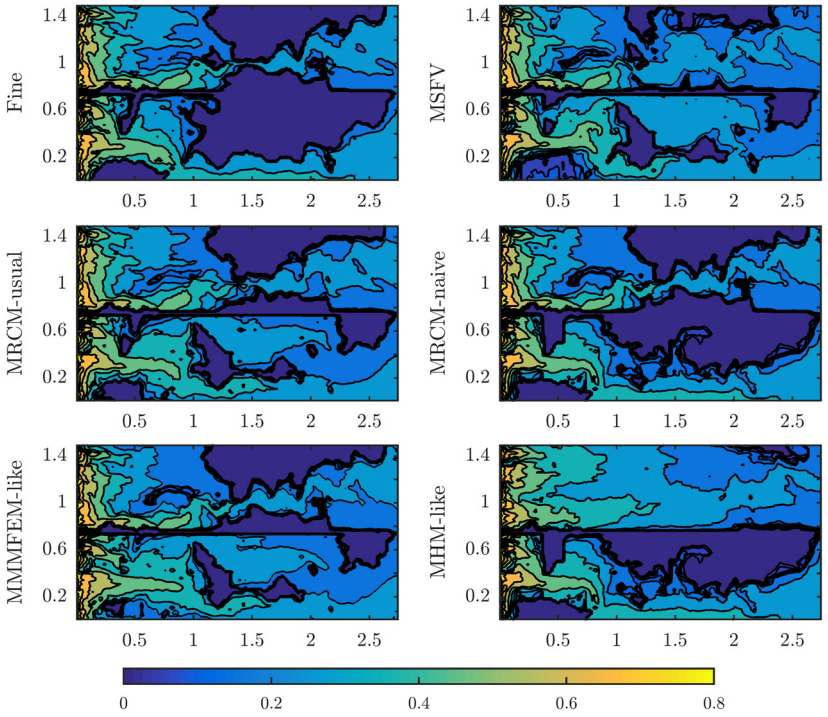

Fig. 16. Saturation profiles at $T_{\text{PVI}} = 0.5$ on the high-contrast permeability field that combines a high permeability channel and a low permeability region. Left column, top to bottom: reference fine grid solution; MRCM-usual saturation profile; MMMFEM-like saturation profile. Right column, top to bottom: MSFV saturation profile; MRCM-naive saturation profile; MHM-like saturation profile. We note that the MRCM-naive approximation is the only method that produces a solution close to the reference saturation map after the breakthrough.

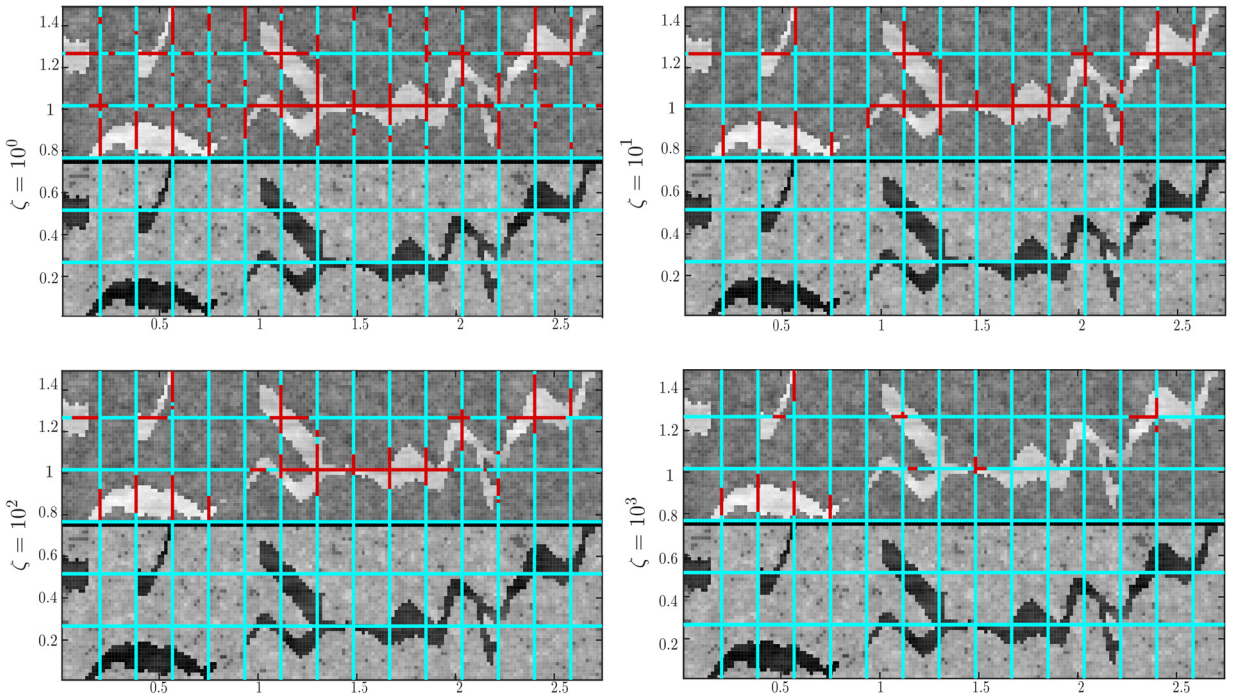

Fig. 17. Choice of the parameter α on subdomain boundaries for the MRCM-adaptive. The red color considers the MMMFEM-like method ($\alpha = 10^{-8}$) on the subdomain boundaries that are in regions of high permeability. The cyan color considers the MHM-like method ($\alpha = 10^{8}$) on the remaining subdomain boundaries. We compare four possibilities for cutoff value ζ. Left column, top to bottom: $\zeta = 10^0$; $\zeta = 10^2$. Right column, top to bottom: $\zeta = 10^1$; $\zeta = 10^3$. The high permeability channel structure is well captured for $\zeta = 10^1$ or $\zeta = 10^2$.

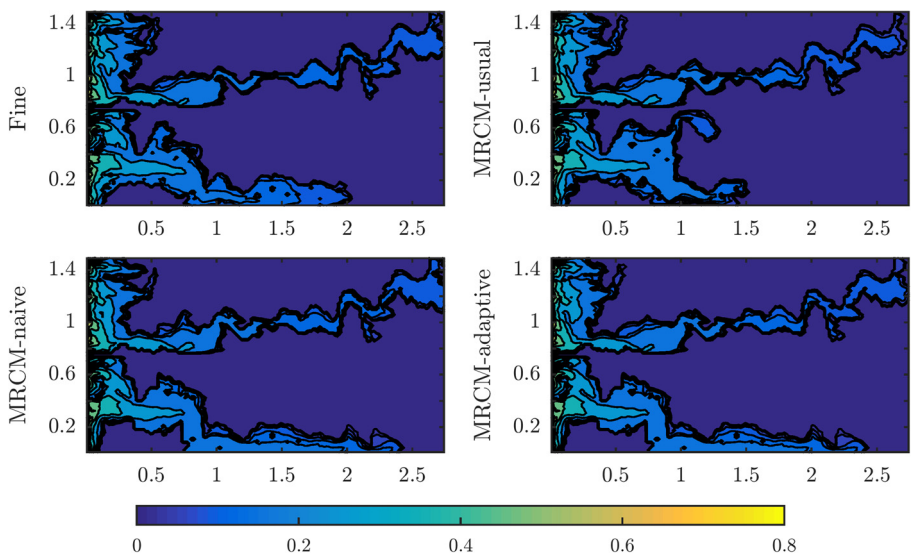

Fig. 18. Comparison of the saturation solutions calculated with the different versions of the MRCM on the high-contrast permeability field that combines a high permeability channel and a low permeability region. Saturation profiles at $T_{\text{PVI}} = 0.06$ (before breakthrough) are shown. Left column, top to bottom: reference fine grid solution; MRCM-naive saturation profile. Right column, top to bottom: MRCM-usual saturation profile; MRCM-adaptive saturation profile. The MRCM-naive and MRCM-adaptive provide more accurate solutions than the MRCM-usual.

the naive and adaptive versions of the MRCM. The saturation results after breakthrough time (illustrated by the dashed line) show smaller errors for these strategies. Note that, in particular, the MRCM-adaptive produces the smallest errors. In summary with the adaptive strategy we have successfully predicted reservoir production in high contrast formations with both channels and obstacles.

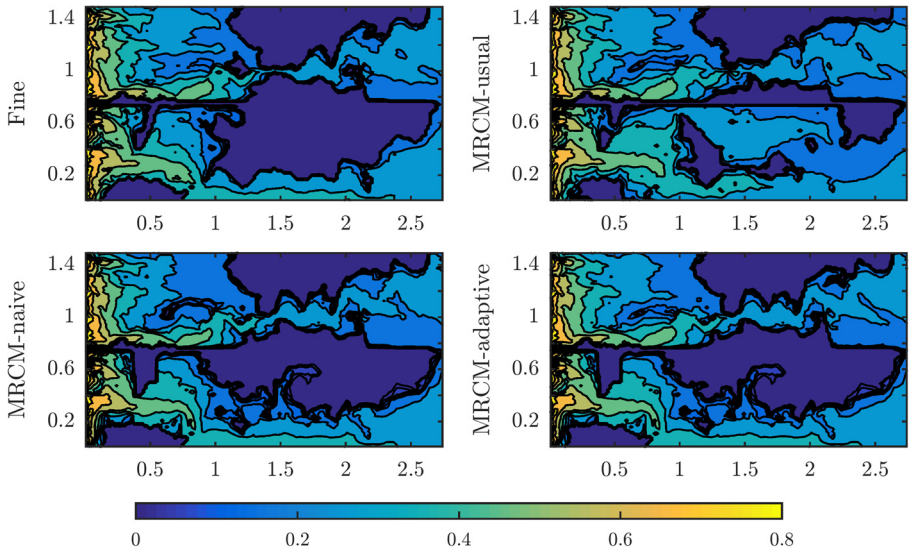

Fig. 19. Comparison of the saturation solutions calculated with the different versions of the MRCM on the high-contrast permeability field that combines a high permeability channel and a low permeability region. Saturation profiles at $T_{\text{PVI}} = 0.5$ are shown. Left column, top to bottom: reference fine grid solution; MRCM-naive saturation profile. Right column, top to bottom: MRCM-usual saturation profile; MRCM-adaptive saturation profile. The MRCM-naive and MRCM-adaptive results remain more accurate than the MRCM-usual after breakthrough.

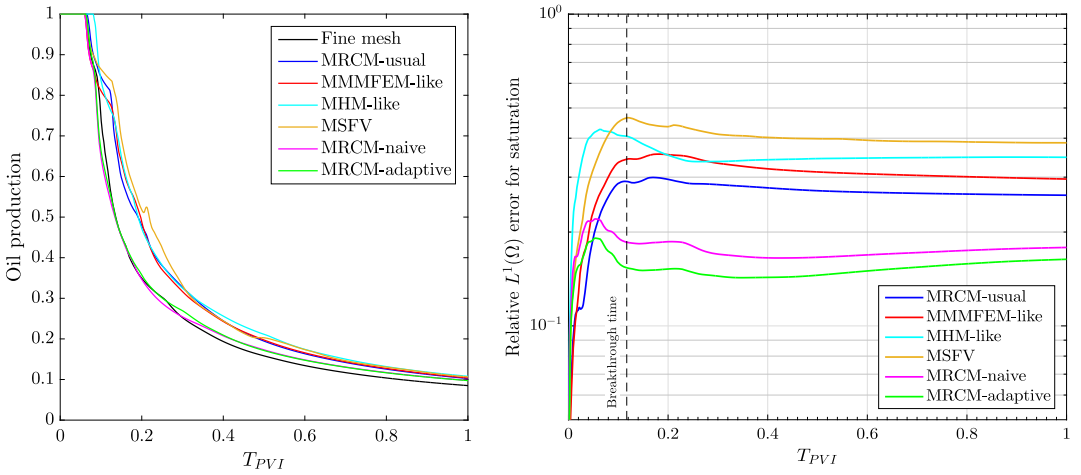

Fig. 20. Oil production curve (left) and relative $L^1(\Omega)$ errors for saturation (right) on the built permeability field as function of time. The breakthrough time is illustrated by dashed line (right plot). We note that the best approximations of oil production curves are performed by the MRCM-naive and MRCM-adaptive. The MRCM-adaptive produces the smallest saturation errors.

5. Conclusions and future work

The Multiscale Robin Coupled method has been carefully investigated for the numerical solution of two-phase, oil-water flows in heterogeneous, high-contrast porous media. The governing system of equations is discretized by an operator splitting technique, such that elliptic equations for velocity and pressure and a hyperbolic conservation law for the water saturation are solved sequentially in time.

Initially we show that, in line with results obtained for single phase flows by some of the authors and their collaborators, the MRCM produces more accurate solutions than other well known multiscale procedures (in terms of global norms of velocity and saturation fields). Then we focus on a detailed investigation of how well multiscale methods approximate oil-water fingering instabilities in very high-contrast, realistic permeability fields. We show that, within multiscale mixed methods, the best scenario for the approximation of these problems involve two well known procedures: the Multiscale Mortar Mixed Finite Element Method (that we show to be appropriate for the approximation of flows in high permeability channels) and the Multiscale Hybrid-Mixed Finite Element Method (that we show to be adequate to handle low permeability regions). By taking advantage of an algorithmic parameter of the MRCM we develop a new adaptivity strategy, such that

depending on the local properties of the permeability field we can easily switch between the known procedures to achieve much better accuracy in comparison with these procedures alone.

The MRCM for two phase flows as presented here can take advantage of state-of-the-art supercomputers, its computational cost is comparable to existing procedures, and the quality of the solutions obtained are clearly better than the ones produced by the standard multiscale methods that we have considered. The authors intend to investigate the use of the MRCM in the implicit solution of multiphase flow and transport problems, possibly including compressibility effects.

Declaration of competing interest

The authors declare that they have no known competing financial interests or personal relationships that could have appeared to influence the work reported in this paper.

Acknowledgements

The authors gratefully acknowledge the financial support received from the Brazilian oil company Petrobras grant 2015/00400-4, and from the São Paulo Research Foundation FAPESP grant CEPID-CeMEAI 2013/07375-0; This study was also financed in part by Brazilian government agencies CAPES (Finance Code 001) and CNPq grant 305599/2017-8; FP was also funded in part by NSF-DMS 1514808, a Science Without Borders/CNPq-Brazil grant 400169/2014-2 and UT Dallas; FFR acknowledges the hospitality provided by UT Dallas; Finally, we thank R.T. Guiraldello for providing the MRCM code and for fruitful discussions about the method.

Appendix A. The Kurganov-Tadmor scheme for two-phase flows

We present the Kurganov-Tadmor method (KT) [44,45] to approximate the solution of scalar conservation laws. Let us consider the hyperbolic conservation law (2) in the form

$$\frac{\partial s}{\partial t} + \frac{\partial}{\partial x}(f(s)\, u^x) + \frac{\partial}{\partial y}(f(s)\, u^y) = 0, \tag{A.1}$$

where $u^x = u^x(x, y, t)$ and $u^y = u^y(x, y, t)$ denote the x and y components of the velocity field $\mathbf{u}$. The spacial finite volume semi-discretization is given by

$$\frac{d}{dt}s_{i,j}(t) = -\frac{1}{\Delta x}\Big(F_{i+1/2,j}(t) - F_{i-1/2,j}(t)\Big) - \frac{1}{\Delta y}\Big(G_{i,j+1/2}(t) - G_{i,j-1/2}(t)\Big), \tag{A.2}$$

where the variable $s_{i,j}(t) = s(x_i, y_j, t)$ is assumed to have a piecewise constant variation over each cell (i, j) at time t. The KT central scheme has discrete fluxes $F_{i-1/2,j}$ on interfaces $x_{i-1/2}$ given by

$$F_{i-1/2,j} = \left(\frac{f(s^-_{i,j}) + f(s^+_{i-1,j})}{2} - \frac{a_{i-1/2,j}}{2}\left(s^-_{i,j} - s^+_{i-1,j}\right)\right) u^x_{i-1/2,j}, \tag{A.3}$$

where $a_{i-1/2,j}$ is an estimate to local speeds of wave propagation on interfaces

$$a_{i-1/2,j} = \max_{s\in[s_{i-1,j}, s_{i,j}]} \big|f'(s)\big|. \tag{A.4}$$

The discrete fluxes $G_{i,j-1/2}$ are calculated in y direction analogously to the $F_{i-1/2,j}$ in x direction.

The saturation solution considers a spatial reconstruction of the form

$$s(x, y, t) = s_{i,j}(t) + \sigma^x_i(x - x_i) + \sigma^y_j(y - y_j), \tag{A.5}$$

for $x_{i-1/2} \le x < x_{i+1/2}$ and $y_{j-1/2} \le y < y_{j+1/2}$. We consider the KT spatial reconstruction given by the limiter function *minmod* [50]:

$$\sigma^x_i = \text{minmod}\left(\frac{s_{i+1,j} - s_{i,j}}{\Delta x}, \frac{s_{i,j} - s_{i-1,j}}{\Delta x}\right) \tag{A.6}$$

and

$$\sigma^y_j = \text{minmod}\left(\frac{s_{i,j+1} - s_{i,j}}{\Delta y}, \frac{s_{i,j} - s_{i,j-1}}{\Delta y}\right), \tag{A.7}$$

where

$$\text{minmod}(a_1, \cdots, a_m) = \begin{cases} \text{sgn}(a_1) \min\limits_{1\leqslant k\leqslant m} \{|a_k|\}, & \text{if } \text{sgn}(a_1) = \cdots = \text{sgn}(a_m) \\ 0, & \text{otherwise} \end{cases}. \tag{A.8}$$

One can observe that if the reconstruction is constant (i.e., $\sigma_i^x = 0 \ \forall \ i$ and $\sigma_j^y = 0 \ \forall \ j$) then this discretization will result in the Rusanov method [53]. In our numerical simulations, Eq. (A.2) is approximated by the classical Forward Euler method.

References

[1] V. Kippe, J. Aarnes, K. Lie, A comparison of multiscale methods for elliptic problems in porous media flow, Comput. Geosci. 12 (3) (2008) 377–398.
[2] P. Jenny, S. Lee, H.A. Tchelepi, Multi-scale finite-volume method for elliptic problems in subsurface flow simulation, J. Comput. Phys. 187 (1) (2003) 47–67.
[3] P. Jenny, S.H. Lee, H.A. Tchelepi, Adaptive multiscale finite-volume method for multiphase flow and transport in porous media, Multiscale Model. Simul. 3 (1) (2005) 50–64.
[4] H. Hajibeygi, D. Karvounis, P. Jenny, A hierarchical fracture model for the iterative multiscale finite volume method, J. Comput. Phys. 230 (24) (2011) 8729–8743.
[5] Y. Wang, H. Hajibeygi, H.A. Tchelepi, Monotone multiscale finite volume method, Comput. Geosci. 20 (3) (2016) 509–524.
[6] D. Cortinovis, P. Jenny, Zonal multiscale finite-volume framework, J. Comput. Phys. 337 (2017) 84–97.
[7] T. Hou, X.-H. Wu, A multiscale finite element method for elliptic problems in composite materials and porous media, J. Comput. Phys. 134 (1997) 169–189.
[8] J. Aarnes, T.Y. Hou, Multiscale domain decomposition methods for elliptic problems with high aspect ratios, Acta Math. Appl. Sin. 18 (1) (2002) 63–76.
[9] T.J. Hughes, G.R. Feijóo, L. Mazzei, J.-B. Quincy, The variational multiscale method - a paradigm for computational mechanics, Comput. Methods Appl. Mech. Eng. 166 (1–2) (1998) 3–24.
[10] Y. Efendiev, J. Galvis, T.Y. Hou, Generalized multiscale finite element methods (GMsFEM), J. Comput. Phys. 251 (2013) 116–135.
[11] A.L. Madureira, M. Sarkis, Hybrid localized spectral decomposition for multiscale problems, arXiv preprint, arXiv:1706.08941.
[12] Y. Efendiev, J. Galvis, X.-H. Wu, Multiscale finite element methods for high-contrast problems using local spectral basis functions, J. Comput. Phys. 230 (4) (2011) 937–955.
[13] Y. Efendiev, S. Lee, G. Li, J. Yao, N. Zhang, Hierarchical multiscale modeling for flows in fractured media using generalized multiscale finite element method, GEM Int. J. Geomath. 6 (2) (2015) 141–162.
[14] N. Zhang, J. Yao, Z. Huang, Y. Wang, Accurate multiscale finite element method for numerical simulation of two-phase flow in fractured media using discrete-fracture model, J. Comput. Phys. 242 (2013) 420–438.
[15] A. Fumagalli, A. Scotti, A numerical method for two-phase flow in fractured porous media with non-matching grids, Adv. Water Resour. 62 (2013) 454–464.
[16] R.T. Guiraldello, R.F. Ausas, F.S. Sousa, F. Pereira, G.C. Buscaglia, The multiscale Robin coupled method for flows in porous media, J. Comput. Phys. 355 (2018) 1–21.
[17] R.T. Guiraldello, R.F. Ausas, F.S. Sousa, F. Pereira, G.C. Buscaglia, Interface spaces for the multiscale Robin coupled method in reservoir simulation, Math. Comput. Simul. 164 (2019) 103–119.
[18] J. Douglas, P. Paes-Leme, J. Roberts, J. Wang, A parallel iterative procedure applicable to the approximate solution of second order partial differential equations by mixed finite element methods, Numer. Math. 65 (1) (1993) 95–108.
[19] A. Francisco, V. Ginting, F. Pereira, J. Rigelo, Design and implementation of a multiscale mixed method based on a nonoveralapping domain decomposition procedure, Math. Comput. Simul. 99 (2014) 125–138.
[20] T. Arbogast, G. Pencheva, M. Wheeler, I. Yotov, A multiscale mortar mixed finite element method, Multiscale Model. Simul. 6 (1) (2007) 319–346.
[21] C. Harder, D. Paredes, F. Valentin, A family of multiscale hybrid-mixed finite element methods for the Darcy equation with rough coefficients, J. Comput. Phys. 245 (2013) 107–130.
[22] R. Araya, C. Harder, D. Paredes, F. Valentin, Multiscale hybrid-mixed method, J. Numer. Anal. 51 (6) (2013) 3505–3531.
[23] Z. Chen, T. Hou, A mixed multiscale finite element method for elliptic problems with oscillating coefficients, Math. Comput. 72 (2003) 541–576.
[24] J. Aarnes, On the use of a mixed multiscale finite element method for greater flexibility and increased speed or improved accuracy in reservoir simulation, Multiscale Model. Simul. 2 (3) (2006) 421–439.
[25] E.T. Chung, Y. Efendiev, C.S. Lee, Mixed generalized multiscale finite element methods and applications, Multiscale Model. Simul. 13 (1) (2015) 338–366.
[26] S. Fu, E. Chung, A local-global multiscale mortar mixed finite element method for multiphase transport in heterogeneous media, arXiv preprint, arXiv:1903.10220.
[27] Y. Yang, E.T. Chung, S. Fu, Residual driven online mortar mixed finite element methods and applications, J. Comput. Appl. Math. 340 (2018) 318–333.
[28] X. Yue, E. Weinan, Numerical methods for multiscale transport equations and application to two-phase porous media flow, J. Comput. Phys. 210 (2) (2005) 656–675.
[29] E.T. Chung, Y. Efendiev, Reduced-contrast approximations for high-contrast multiscale flow problems, Multiscale Model. Simul. 8 (4) (2010) 1128–1153.
[30] H. Zhou, H.A. Tchelepi, Two-stage algebraic multiscale linear solver for highly heterogeneous reservoir models, SPE J. 17 (02) (2012) 523–539.
[31] O. Møyner, K.-A. Lie, A multiscale restriction-smoothed basis method for high contrast porous media represented on unstructured grids, J. Comput. Phys. 304 (2016) 46–71.
[32] Y. Efendiev, V. Ginting, T. Hou, R. Ewing, Accurate multiscale finite element methods for two-phase flow simulations, J. Comput. Phys. 220 (1) (2006) 155–174.
[33] M. Presho, J. Galvis, A mass conservative generalized multiscale finite element method applied to two-phase flow in heterogeneous porous media, J. Comput. Appl. Math. 296 (2016) 376–388.
[34] J.E. Aarnes, S. Krogstad, K.-A. Lie, A hierarchical multiscale method for two-phase flow based upon mixed finite elements and nonuniform coarse grids, Multiscale Model. Simul. 5 (2) (2006) 337–363.
[35] F. Furtado, V. Ginting, F. Pereira, M. Presho, Operator splitting multiscale finite volume element method for two-phase flow with capillary pressure, Transp. Porous Media 90 (3) (2011) 927–947.
[36] P. Jenny, S.H. Lee, H.A. Tchelepi, Adaptive fully implicit multi-scale finite-volume method for multi-phase flow and transport in heterogeneous porous media, J. Comput. Phys. 217 (2) (2006) 627–641.
[37] B. Ganis, K. Kumar, G. Pencheva, M.F. Wheeler, I. Yotov, A global Jacobian method for mortar discretizations of a fully implicit two-phase flow model, Multiscale Model. Simul. 12 (4) (2014) 1401–1423.
[38] J. Douglas, R. Ewing, M. Wheeler, A time-discretization procedure for a mixed finite element approximation of miscible displacement in porous media, RAIRO. Anal. Numér. 17 (3) (1983) 249–265.
[39] J. Douglas, F. Furtado, F. Pereira, On the numerical simulation of waterflooding of heterogeneous petroleum reservoirs, Comput. Geosci. 1 (2) (1997) 155–190.
[40] J. Douglas, F. Pereira, L.-M. Yeh, A locally conservative Eulerian–Lagrangian numerical method and its application to nonlinear transport in porous media, Comput. Geosci. 4 (1) (2000) 1–40.
[41] T. Arbogast, Implementation of a locally conservative numerical subgrid upscaling scheme for two-phase Darcy flow, Comput. Geosci. 6 (3–4) (2002) 453–481.

[42] M.G. Edwards, A higher-order Godunov scheme coupled with dynamic local grid refinement for flow in a porous medium, Comput. Methods Appl. Mech. Eng. 131 (3–4) (1996) 287–308.
[43] E. Abreu, F. Pereira, S. Ribeiro, Central schemes for porous media flows, Comput. Appl. Math. 28 (1) (2009) 87–110.
[44] A. Kurganov, E. Tadmor, New high-resolution central schemes for nonlinear conservation laws and convection–diffusion equations, J. Comput. Phys. 160 (1) (2000) 241–282.
[45] S.M. Damián, N.M. Nigro, G.C. Buscaglia, A central scheme for advecting scalars by velocity fields obtained from finite volume multiphase incompressible solvers, Appl. Math. Model. 40 (15) (2016) 6934–6955.
[46] D.W. Peaceman, Fundamentals of Numerical Reservoir Simulation, vol. 6, Elsevier, 2000.
[47] R.E. Ewing, The Mathematics of Reservoir Simulation, SIAM, 1983.
[48] R.T. Guiraldello, R.F. Ausas, F.S. Sousa, F. Pereira, G.C. Buscaglia, Velocity postprocessing schemes for multiscale mixed methods applied to contaminant transport in subsurface flows, Comput. Geosci. (2020), https://doi.org/10.1007/s10596-019-09930-8.
[49] Z. Chen, G. Huan, Y. Ma, Computational Methods for Multiphase Flows in Porous Media, vol. 2, SIAM, 2006.
[50] R.J. LeVeque, Finite Volume Methods for Hyperbolic Problems, vol. 31, Cambridge University Press, 2002.
[51] M.A. Christie, M.J. Blunt, Tenth SPE comparative solution project: a comparison of upscaling techniques, in: SPE Reservoir Simulation Symposium, Society of Petroleum Engineers, 2001.
[52] I. Lunati, S.H. Lee, An operator formulation of the multiscale finite-volume method with correction function, Multiscale Model. Simul. 8 (1) (2009) 96–109.
[53] V.V. Rusanov, The calculation of the interaction of non-stationary shock waves and obstacles, USSR Comput. Math. Math. Phys. 1 (2) (1962) 304–320.